International Journal of Machine Tools & Manufacture 178 (2022) 103906

Contents lists available at ScienceDirect

International Journal of Machine Tools and Manufacture

journal homepage: www.elsevier.com/locate/ijmactool

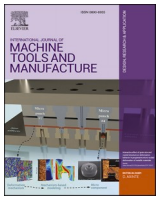

# Surface integrity and material removal mechanisms in high-speed grinding of Al/SiCp metal matrix composites

Sai Guo [a,b], Shouxiang Lu [a], Bi Zhang [a,*], Chi Fai Cheung [b,**]

[a] Department of Mechanical and Energy Engineering, Southern University of Science and Technology, Shenzhen, 518055, China
[b] State Key Laboratory of Ultraprecision Machining Technology, Department of Industrial and Systems Engineering, The Hong Kong Polytechnic University, Kowloon, Hong Kong, China

ARTICLE INFO

*Keywords:*
Surface integrity
High-speed grinding
Al/SiCp
Subsurface damage
Material removal mechanisms
Ultra-precision machining

ABSTRACT

SiC particle reinforced Al metal matrix composites (Al/SiCp MMCs) are typical difficult-to-machine materials due to the heterogeneous constituent. Poor surface integrity is commonly caused in conventional machining methods. To explore material removal mechanisms in high-speed grinding, this study carries out high-speed grinding (HSG) on an Al/SiCp MMC at a grinding speed from 30.4 m/s to 307.0 m/s, and assesses surface integrity including surface damage and subsurface damage (SSD) to explore how different grinding speeds take effect therein. The results reveal that improved surface quality is attained in HSG in which continuous and discontinuous dynamic recrystallization mechanisms govern Al grain refinement, and the latter is inclined to occur in the upper part of the ground surface. The distribution of the O-rich zone is closely associated with subsurface cracks. The workpiece ground at a higher grinding speed is with less damage than at a lower grinding speed due to the reduced O-rich zone. Three different layers in the subsurface below ground workpiece are identified based on various features, which are relatively narrower compared to that in low-speed grinding. The range of plastic deformation of the Al alloy matrix is suppressed in HSG because of larger Al grains and a reduced depth of lateral cracks in Al alloy matrix. Distinctly denser dislocation kinks formed at the boundary of SiC particles in HSG indicate the increased ductility of SiC particles. In HSG of Al/SiCp MMCs, strain-rate effect prevails for Al alloy matrix as a result of reduced ductility, and size effect plays the dominant role for SiC particles due to increased ductility, which facilitate reducing the property discrepancies between these two very different components. Therefore, an improved surface integrity of the Al/SiCp MMCs is realized through HSG. This study enhances the understanding of the surface and subsurface formation and material removal mechanisms in HSG of Al/SiCp MMCs, which can provide a theoretical basis and practical reference for achieving better surface quality for Al/SiCp MMCs and other composites machined by HSG.

## 1. Introduction

SiC particle reinforced Al metal matrix composites (Al/SiCp MMCs) represent a new generation of materials featuring significant scientific, technological, and commercial importance [1–3] owing to their high specific strength and stiffness, high temperature resistance, and exceptional corrosion resistance compared to their equivalent non-reinforced metallic alloys [4–6]. Al/SiC MMCs are hence being used to replace conventional materials in various engineering applications in aerospace, aircraft, electronics, and automotive industries due to the increasing performance requirements [7,8]. However, Al/SiCp MMCs are notoriously known to be typical difficult-to-machine materials when the conventional cutting or milling techniques are utilized for Al/SiCp MMCs because of the marked property difference between the two constituents of hard ceramic reinforcement (SiC particles) and ductile metal matrix (Al alloy matrix). To be specific, the heterogeneous structure always leads to serious surface defects and subsurface damage (SSD) in a conventional machining process [9–11], which substantially deteriorates the mechanical characteristics and fatigue properties of the machined materials [12].

In machining of Al/SiCp MMCs, surface pits, cracks, and scratches are the typical defects of the machined surface due to the

* Corresponding author.
** Corresponding author.
*E-mail addresses:* zhangb@sustech.edu.cn (B. Zhang), benny.cheung@polyu.edu.hk (C.F. Cheung).

https://doi.org/10.1016/j.ijmachtools.2022.103906
Received 20 December 2021; Received in revised form 1 June 2022; Accepted 4 June 2022
Available online 7 June 2022

inhomogeneous structure of the materials, which is governed by different material removal mechanisms of both the soft Al alloy matrix and the hard SiC particles [13]. In machining of the Al alloy matrix, a conventional process may suffer from cutting tool wear, built-up edges, and workpiece burn because of severe plastic deformation [14]. In machining of SiC particles, brittle fracture along with cracks and fragments is commonly the mechanism dominating brittle material removal. Moreover, the relative position of the cutting tool and the SiC particles plays a vital role in determining the quality of surface integrity of machined surface [15]. To be specific, the relative position when the tool are located at upper, lower, or middle part of an SiC particle corresponds to five different surface damage modes, i.e., fracture, press-in, pull-out, rotation, and ploughing of SiC particles [16]. When there is no interaction between the tool and SiC particle, the cutting mechanism can be attributed to shearing of the ductile Al alloy matrix [1]. Since both ductile removal and brittle removal mechanisms co-exist in machining of Al/SiCp MMCs, the machined surface contains the surface damage modes that are specific to the combination of the two very different components. Although extensive studies have been performed on the surface quality in machining of Al/SiCp MMCs through evaluating the effects of different machining methods and process parameters on the surface quality [6,17,18] and SSD [1,4,19]. Few of the current works are focused on material removal mechanisms. Therefore, an in-depth investigation on SSD is needed to reveal material removal mechanisms and improve surface integrity of Al/SiCp MMCs.

In a practical machining process, the surface damage modes and surface integrity are not only influenced by the corresponding material removal mechanisms, but also associated with the influence of thermal effect in the machining zone. As a typical difficult-to-machine material, Al/SiCp MMC is known to have a high temperature rise during a conventional machining process because of severe plastic deformation of the Al alloy matrix and intense tool-chip friction. The extensive plastic deformation and thermal effect in the machining zone bring about many practical problems [1,2]. On one hand, heat generation causes dimensional inaccuracies to the workpiece due to the intense thermal expansion [4]. On the other hand, adhesion of the workpiece material to the machining tool usually occurs in machining of ductile Al alloy, thus increasing machining forces and consequently temperature rise in the machining zone [8]. Moreover, higher levels of diffusion and oxidation may occur to the machined surface when subjected to larger thermal loads, which can further deteriorate the surface integrity of the workpiece. With increasing the machining speed, it is believed that thermal effect will become more pronounced due to more intense friction and plastic deformation. However, it is quite difficult to directly measure the temperature rise in the machining zone, especially in a high-speed machining process.

To deal with the problems faced by the conventional machining of Al/SiCp MMCs, great efforts have been devoted to developing high-speed grinding (HSG) method, i.e., grinding at a speed of 10–15 times higher than its conventional counterparts. Compared with other machining methods, HSG is more feasible to simultaneously achieve high-efficiency, high-accuracy, and low-damage machining [20]. In HSG, the material deformation and removal mechanisms can be different from that in conventional machining because of high strain-rate evoked material embrittlement and the significantly reduced thermal effect resulted from the suppression of plastic strains in the machining zone [21,22]. The interplay of thermal effect, size effect, and strain-rate effect in an HSG process complicates the analysis of surface defects and SSD. Moreover, the inhomogeneous microstructure of Al/SiCp MMCs further increases the complexity in analyzing surface integrity and the corresponding material removal mechanisms. At present, there has not been significant research on exploring the material removal mechanisms at such high grinding speeds considering the complicated interplay of these factors as well as great property discrepancies of the two components of Al/SiCp MMCs through HSG.

Although HSG of Al/SiCp MMCs are rarely reported, studies on HSG of other materials are extensively investigated. Shimizu et al. [23] revealed evident work hardening and improved surface quality in HSG of Al. In HSG of the Al6060T6 alloy, Guo et al. concluded that an increased grinding speed was beneficial to improving surface integrity through weakening surface plastic deformation and reducing the depth of SSD [24]. As reported by Choudhary et al. [25], a drastic reduction in SSD was observed in HSG of alumina. In an HSG study of zirconia, Chen et al. [26] found that the dominating removal mechanism changed from brittle to ductile at an increased grinding speed. It is speculated that HSG will improve grindability of both ductile and hard materials, as well as the composite materials made of both ductile matrix and hard reinforcements. With a rapid development of high-speed precision machine tools, HSG of Al/SiCp MMCs at a maximum linear speed of over 300 m/s has currently become a reality, which is yet to be investigated.

To investigate the surface integrity and material removal mechanisms in grinding of Al/SiCp MMCs, reliable and accurate methods for SSD characterization are beneficial to improving the reliability of experimental results. For revealing SSD, mechanical polishing [13,27] and chemical etching [1] are the widely employed methods. However, the veracity of the results would be substantially compromised once original damage is impaired or additional damage is introduced by using these methods, which will undermine the accuracy of experimental results and prediction models. To improve the reliability of SSD characterization, the in-situ etching by focused ion beam (FIB) is adopted to delicately capture SSD information without introducing extraneous damage to a sample [28]. FIB milling has widely been used in materials science to produce thin lamellae for transmission electron microscopy (TEM). It is an ideal technique to reveal SSD in HSG of Al/SiCp MMCs.

In HSG of Al/SiCp MMCs, a critical problem is how the components of Al/SiCp MMCs respond to grinding at a high strain-rate but a small cutting depth. Up to now, there has not been any significant research on HSG of Al/SiC MMCs considering the respective material responses and material removal mechanisms in HSG. Moreover, it is difficult to find a reliable method for comprehensively evaluating surface integrity without introducing additional damage, especially for the SSD evaluation.

This study carries out high-speed grinding on Al/SiCp MMCs at a grinding speed up to 307.0 m/s, and assesses surface integrity and material removal mechanisms, including surface and subsurface damage, as well as material ductile-to-brittle transition at critical grinding speeds. A comprehensive analysis will be conducted to elaborate surface integrity and material removal mechanisms at the subgrain scale, material deformation behaviors and SSD formation mechanisms for different components of Al/SiCp MMCs in HSG.

## 2. Workpiece materials and experimental procedures

### 2.1. Workpiece materials

The Al/SiCp MMC was used as workpiece material in this study, and was comprised of 35 vol% SiC particles in the AlSi12 alloy matrix. The chemical compositions of the AlSi12 alloy are listed in Table 1. The workpiece material was fabricated via a powder metallurgy route. After fabrication, a workpiece was ground and polished using diamond abrasive papers into a block with dimensions of 10 mm × 10 mm × 5 mm for the subsequent grinding experiments.

Fig. 1a shows the size distribution of the reinforced SiC particles, where the average size of the SiC particles was determined as 14.4 μm by a laser particle size analyzer (Mastersizer 3000, Malvern, UK). The insert in Fig. 1a shows that irregularly shaped SiC particles were randomly distributed in the AlSi12 alloy matrix. Minor voids identified in the interfaces between these two phases were considered normal due to the incomplete compaction during the fabrication process. The phase constituents of the Al/SiCp MMC were characterized using the X-ray diffraction (XRD) technique as shown in Fig. 1b, which were composed of four main phases, i.e., Si, 6H–SiC, 3C–SiC, and Al.

**Table 1**
Chemical compositions of the AlSi12 alloy matrix.

| Element | Al | Si | Fe | Mg | Cu | Zn | Ti | Mn |
|---|---|---|---|---|---|---|---|---|
| wt% | Balance | 11.7 | 0.11 | <0.01 | ≤0.01 | ≤0.01 | ≤0.01 | ≤0.01 |

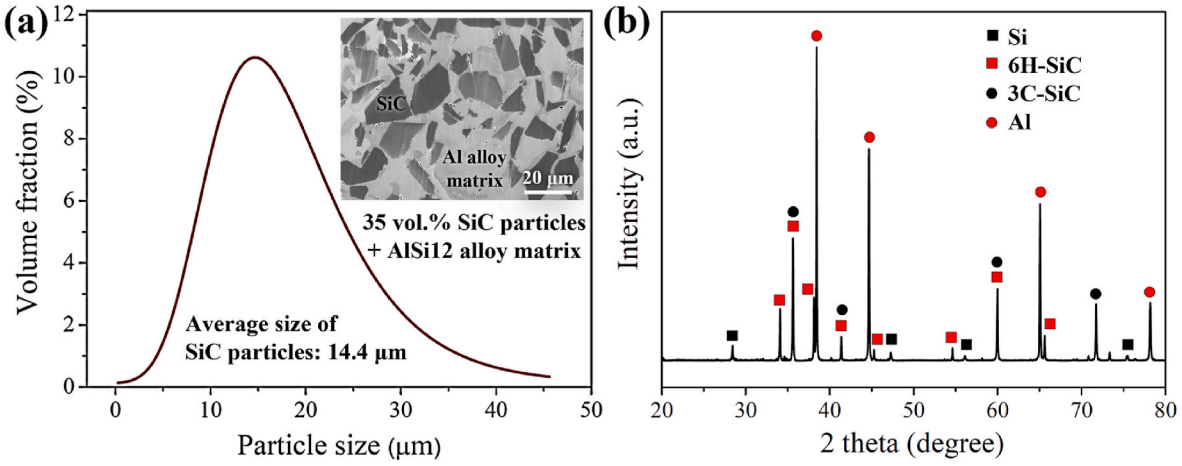


**Fig. 1.** (a) Size distribution of the SiC particle, and (b) phase constituents of the Al/SiCp MMC.

### 2.2. Experimental setup

In this study, HSG of the Al/SiCp MMC was carried out on a grinding machine (Quest GT27, Hardinge, USA) which was equipped with a customized high-speed hydrostatic motorized spindle (TDM SA, Switzerland) as shown in Fig. 2a. The spindle was able to reach a rotational speed up to 60,000 rpm with a radial/axial error motion less than 0.1 μm, a power up to 12.5 kW, a radial stiffness over 40 N/μm, and a

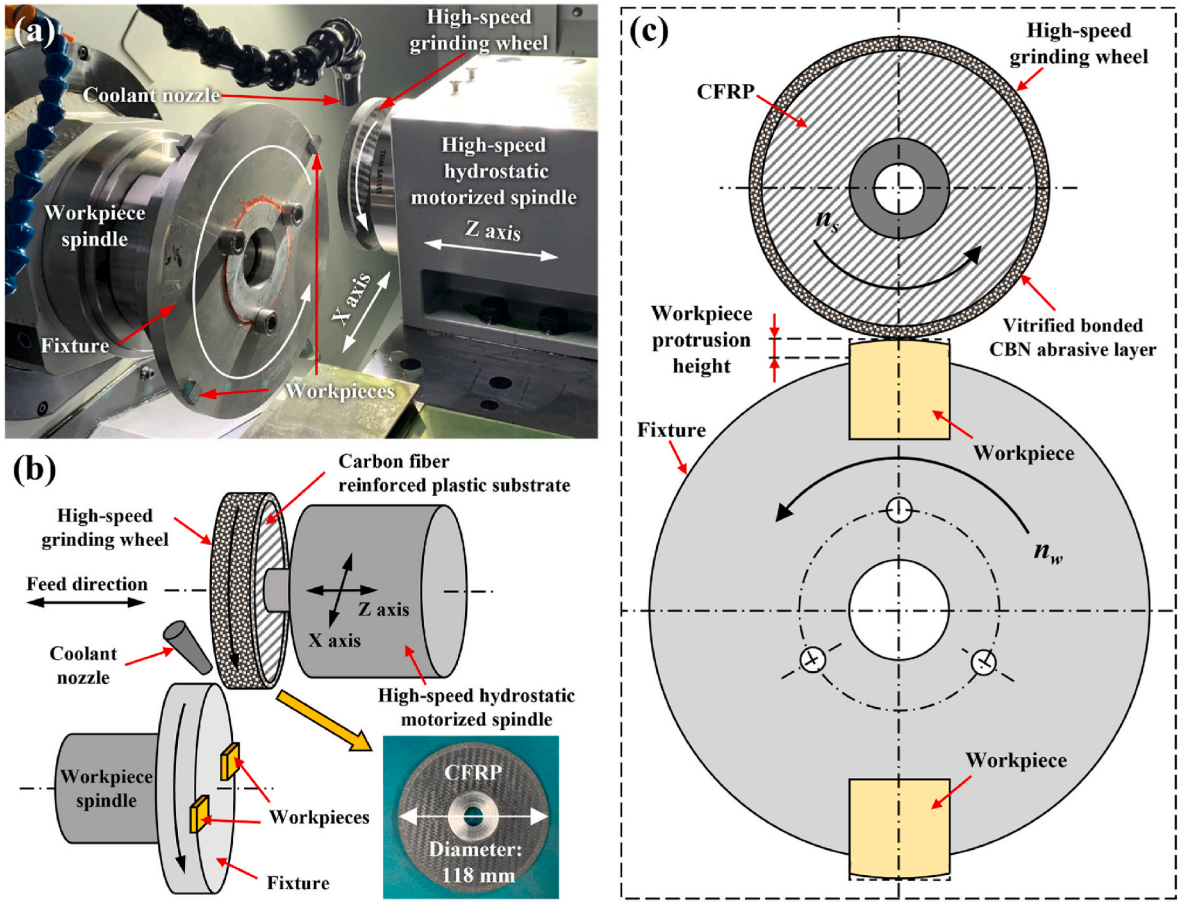


**Fig. 2.** (a) Experimental setup for HSG arrangement of the Al/SiCp MMC; (b), (c) schematic diagrams from different perspectives.

radial load capacity over 380 N. A carbon fiber reinforced CBN grinding wheel was used in the HSG study.

Al/SiCp MMC workpieces were attached to the workpiece spindle of the HSG machine. A workpiece fixture of a diameter of 190 mm and a thickness of 8 mm was mounted to the workpiece spindle, shown in Fig. 2b. Two identical workpieces were symmetrically fixed to the periphery of the fixture using paraffin wax to maintain high stiffness and dynamic balance. After being attached to the fixture, a dead weight of 1 kg was hanged to the workpiece to assess the reliability of paraffin wax. To facilitate a successful grinding, the workpieces were placed with a protrusion length of 2 mm on the periphery of the fixture, as schematically shown in Fig. 2c. To improve the damping characteristics of the grinding wheel with a reduced weight, a carbon fiber reinforced plastic (CFRP) disc was designed to serve as the substrate and vitrified bonded CBN abrasives were used for the high-speed grinding wheel fabrication. The high-speed grinding wheels used in this study were cooperatively fabricated by a professional manufacturer (Zhengzhou Research Institute for Abrasives & Grinding, China). The detailed information of the grinding wheels is presented in Table 2.

### 2.3. Experimental procedures

Prior to each grinding trial, the grinding wheel was first trued with a #800 diamond rolling wheel. During the trueing process, the feed rate along the X axis was 200 mm/min, and the trueing depth was 0.5 μm per pass. The grinding wheel and the diamond rolling wheel were rotated in the same direction at 22,000 rpm and 5,000 rpm, respectively. After trueing, the grinding wheel was dressed with a #800 SiC wheel by contacting the rotating grinding wheel for about 30 s. The dressing parameters were the same as those for trueing. A water-based coolant was employed in the trueing and dressing processes via flood cooling with a flow rate of 10 L/min. The wheel was then balanced at the grinding speed being used during each test using a dynamic balancing instrument (BMT240M.2, MPM, Germany). HSG of the Al/SiCp MMC was performed according to the parameters tabulated in Table 3 where seven trials were designed to investigate the effect of grinding speed up to 307.0 m/s on the surface integrity and material removal mechanisms. Since up-grinding was performed in this study, i.e., the grinding wheel and workpiece rotated in the same direction, the relative linear grinding speed $v_g$ is expressed as $v_g = v_s + v_w$, where $v_s$ and $v_w$ are the linear speed of the grinding wheel and workpiece, respectively.

For each trial, the flat surface of the workpiece facing the wheel was gradually ground into a cylindrical surface as show in Fig. 2c, then a further workpiece depth of 500 μm was removed to expose the fresh material and retain the features induced by this set of grinding parameters. In the meanwhile, a water-based coolant was employed in the grinding process via flood cooling with a flow rate of 10 L/min to reduce friction and temperature rise. In addition, triple replicated experiments for each trial were performed for achieving a high reliability of the experimental results.

**Table 2**
Parameters of the high-speed grinding wheel.

| Item | Description |
|---|---|
| Manufacturer | Zhengzhou Research Institute for Abrasives & Grinding, China |
| Substrate | CFRP |
| Abrasive layer | Vitrified bonded CBN |
| Mesh size | #120 (average grit size of 124 μm) |
| Diameter (mm) | 118 |
| Thickness (mm) | 10 |
| Wheel concentration (%) | 175 |

### 2.4. Measurement and material characterization

After grinding, the surface morphology was observed with a scanning electron microscope (SEM, Merlin, Zeiss, Germany). The three-dimensional topography of the ground surfaces was obtained by using a white light interferometer (Taylor Hobson Talysurf CCI, USA) in which surface roughness parameters *Sa* and *Sz*, together with line roughness parameters *Ra* and *Rz*, were directly measured. To observe SSD at different scales, two methods were adopted, i.e., the ion beam imaging method of the cross-section after the FIB in-situ etching, and the TEM analysis method of the cross-sectional lamellar specimens prepared using the FIB milling. As for the first method, the FIB in-situ etching was performed as shown in Fig. 3, on Helios Nanolab 600i (FEI, USA) to expose the cross-section along the grinding direction (see Fig. 3a), which could retain the pristine damage features (see Fig. 3b) without introducing extraneous damage. For the second method, the cross-sectional lamellae for TEM analysis were prepared using the FIB milling, as shown in Fig. 3c, and then investigated by TEM (Talos F200X G2, FEI, USA). Moreover, the high-angle annular dark-field (HAADF) and energy dispersive spectroscopy (EDS) images of TEM specimens were captured to investigate the elemental distribution. All the TEM specimens were coated with a protective carbon layer before the FIB operation to prevent the surfaces from the gallium ion bombardment during the process.

In addition, triple replicated measurements were performed to achieve a high reliability of the measurement results. For surface and subsurface microstructure observations, representative figures were adopted to compare the differences subjected to different grinding conditions.

## 3. Results

### 3.1. Surface damage

As shown in Fig. 4a, the surface prepared via ion polishing served as the control in this study, which distinctly featured irregularly shaped SiC particles (dark grey) randomly dispersed in the Al alloy matrix (light grey). At the grinding speed of $v_g = 30.4\ m/s$ as displayed in Fig. 4b, surface defects including grinding scratches, surface pits, and fragments were the main features as a result of drastic plastic deformation and broken SiC particles induced by the grinding actions. With an increase in grinding speed from $v_g = 30.4\ m/s$ to $v_g = 133.5\ m/s$ (Fig. 4b–e), the surface morphology did not have much change. However, as the grinding speed was further increased to $v_g = 213.8 m/s$ (Fig. 4f), $v_g = 272.3\ m/s$ (Fig. 4g), and $v_g = 307.0 m/s$ (Fig. 4h), grinding scratches became unobservable, and less and smaller surface pits emerged, which indicated the improved surface quality.

To quantitatively characterize the variations in surface morphology, surface roughness parameters were captured to evaluate the effect of grinding speed on surface damage. As shown in Fig. 5a, surface damage was clearly identified in terms of surface pits and grinding scratches. With increasing the grinding speed, the variations in surface topography can be summarized as follows: as the pits become smaller and shallower, the grinding scratches gradually become inconspicuous, and the dominant tone of the images turned from brown to dark green, which indicated a gradual decrease in surface roughness. The corresponding surface roughness parameters in Fig. 5b,c are consistent with the variation trend of the surface topography. All the surface roughness parameters show a similar trend of an approximate 50% decrease as grinding speed increased from $v_g = 30.4\ m/s$ to $v_g = 307.0\ m/s$.

### 3.2. SSD

In order to reveal the microstructure alterations of the subsurface layer after grinding, cross-sectional observations were conducted to expose SSD of the ground workpiece using the FIB milling and TEM

**Table 3**
Parameters for HSG processes of Al/SiCp MMC.

| Grinding trial # | | 1 | 2 | 3 | 4 | 5 | 6 | 7 |
|---|---|---|---|---|---|---|---|---|
| Grinding wheel | Rotational speed $n_s$ (rpm) | 3,310 | 6,613 | 10,012 | 19,993 | 32,996 | 36,005 | 40,000 |
| | Linear speed $v_s$ (m/s) | 20.4 | 40.8 | 61.8 | 123.5 | 203.8 | 222.3 | 247.0 |
| Workpiece | Rotational speed $n_w$ (rpm) | 1,000 | 1,000 | 1,000 | 1,000 | 1,000 | 5,000 | 6,000 |
| | Linear speed $v_w$ (m/s) | 10 | 10 | 10 | 10 | 10 | 50 | 60 |
| Grinding depth $a_p$ (μm) | | 2.5 | 2.5 | 2.5 | 2.5 | 2.5 | 2.5 | 2.5 |
| Axial feed rate $v_f$ (mm/min) | | 100 | 100 | 100 | 100 | 100 | 100 | 100 |
| Grinding speed $v_g$ (m/s) | | 30.4 | 50.8 | 71.8 | 133.5 | 213.8 | 272.3 | 307.0 |

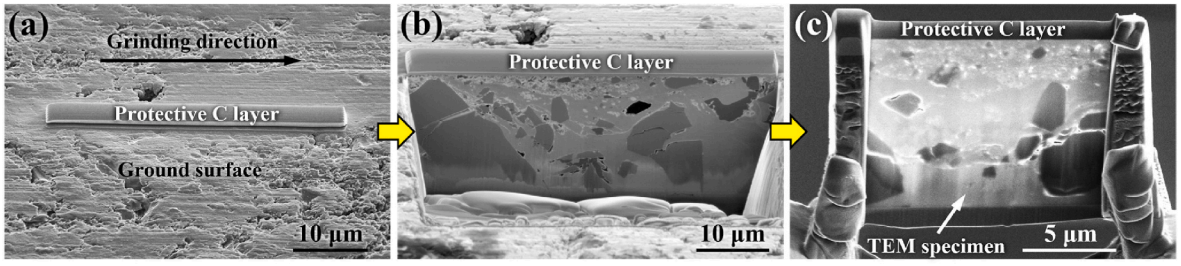


**Fig. 3.** FIB milling and TEM specimen preparation: (a) location of the cross-section milled by FIB; (b) cross-section observed via ion beam imaging; (c) FIB milled TEM specimen.

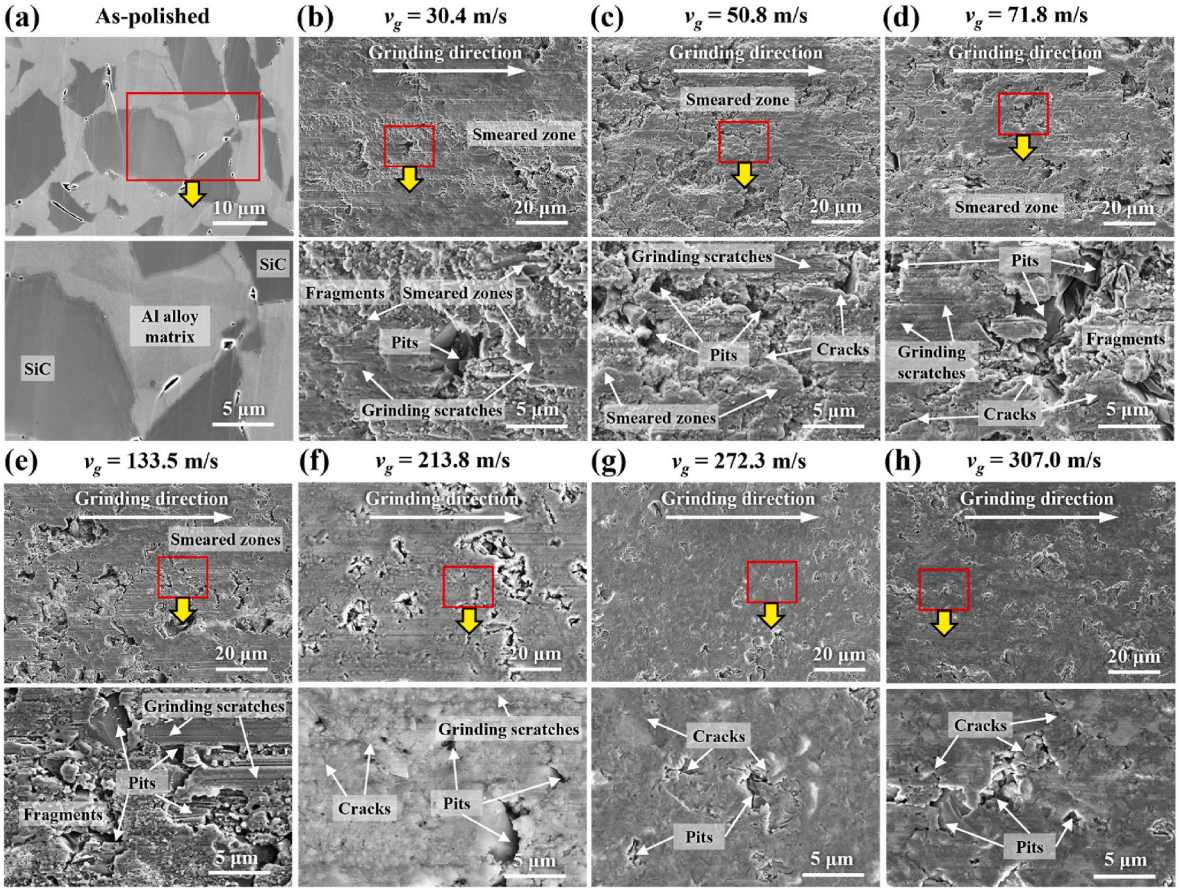


**Fig. 4.** Surface morphology comparison of the Al/SiCp MMC workpieces ground at various grinding speeds: (a) as-polished surface; (b–h) ground surfaces at various speeds. The surface damage reduction indicating the improved surface quality at an increased grinding speed.

techniques. As shown in Fig. 6a, the representative cross-sectional image of the polished workpiece prior to grinding showed a high polishing quality, from which only a deformed Al alloy matrix layer of less than 1 μm in thickness was revealed without significant damage identified in the SiC particles. It is worth mentioning that no distinct Al alloy grain boundaries were observed in Fig. 6a, which indicates that the original grain size of the Al alloy matrix was likely to be larger than 10 μm. However, the subsurface after grinding at $v_g = 30.4\,m/s$ was revealed

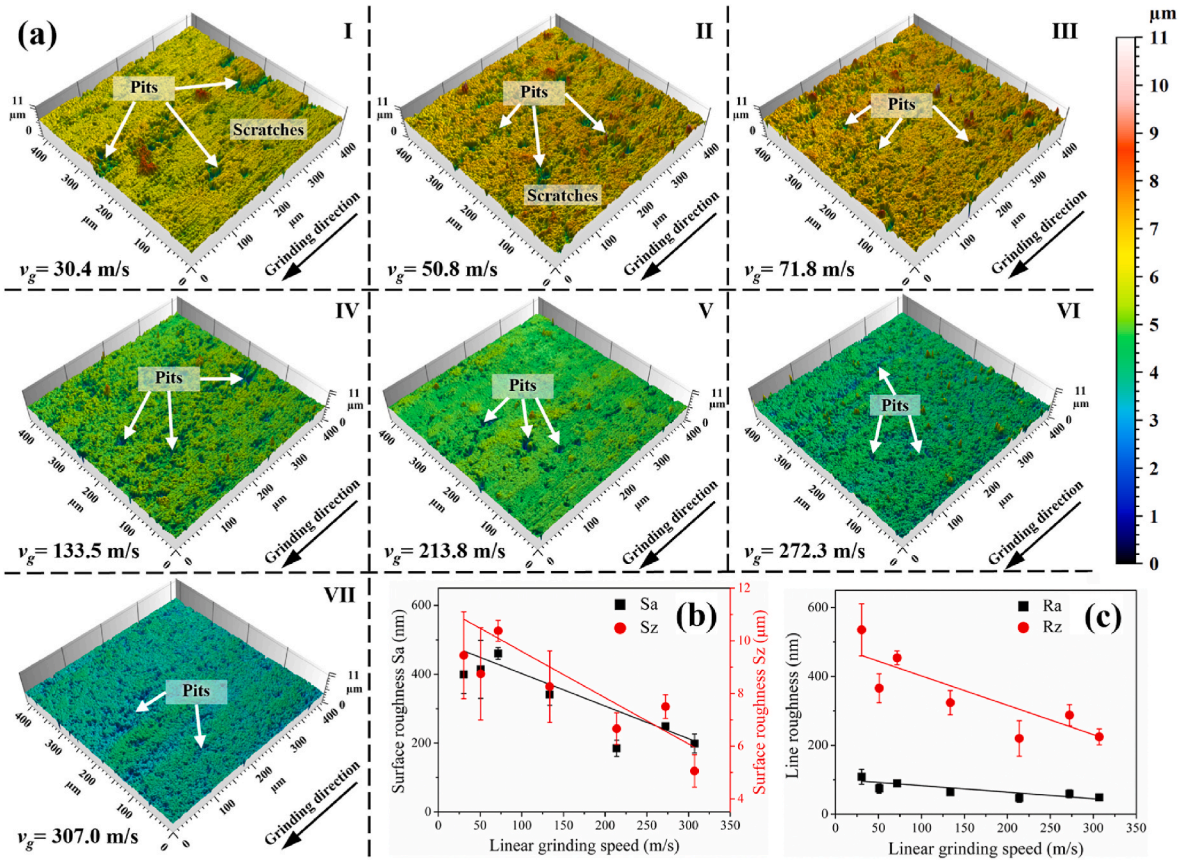


**Fig. 5.** (a) Three-dimensional surface topography of the ground surfaces; (b) surface roughness parameters *Sa* and *Sz*; (c) line roughness parameters *Ra* and *Rz*. A decreasing surface roughness with an increase in grinding speed, indicating improved surface quality.

with distinct SSD, as displayed in Fig. 6b. It can be identified that the fractured and fragmentary SiC particles in a size of about 1 μm were mixed with highly refined Al grains in the top part of the cross-section. In the lower part of the cross-section, larger broken SiC particles with evident cracks were revealed accompanied with many lateral cracks in the Al alloy matrix due to severe shearing effect induced by impacting of SiC particles. In this part, refined Al alloy matrix emerged as typical SSD features besides the broken SiC particles and refined Al grains. Below the lateral cracks in the Al alloy matrix, elongated and larger Al grains were found due to less intense plastic deformation. As the grinding speed further increased to $v_g = 133.5\,m/s$ and $v_g = 307.0\,m/s$, similar phenomena to those ground at $v_g = 30.4m/s$ were found as shown in Fig. 6c,d, both featuring broken SiC particles surrounded by deformed and refined Al alloys, as well as evident lateral cracks in the Al alloy matrix. The observations shown in Fig. 6 indicate an experimental evidence that large Al grains and lower depth of lateral cracks in the Al alloy matrix exist in the subsurface layer of the workpiece ground at a high speed than at a low speed. In other words, better surface integrity was obtained at a higher grinding speed.

TEM analysis was further carried out to investigate SSD of the cross-sections of the ground workpiece, shown in Fig. 7. HAADF images and EDS images were captured to differentiate the SiC particles from the Al alloy matrix, and identify the distribution of the O-element in the cross-sections. The shape and size of the SiC particles were clearly revealed according to the element distribution maps. Lateral cracks indicated with yellow arrows in the Al alloy matrix were distributed at a smaller depth in the ground subsurface at an increased grinding speed, which reflected the reduced plastic deformation of the Al alloy matrix.

As for the element maps, it is worth noticing that the occurrence of the O-element was coincident with the cracks and boundaries of the SiC particles, cracks in the Al alloy matrix, interface between the SiC particles and the Al alloy matrix, as well as the fragmentary SiC particles in the top part of the cross-sections. In order to clarify the composition of the O-rich zone, selective area electron diffraction (SAED) patterns were utilized to identify the crystal structure. It is revealed that the O-rich zone in Fig. 7a comprised of FCC-Al and FCC-Si, without any other noticeable phases. While for the O-rich zone in Fig. 7b,c, the corresponding SAED patterns identified the existence of FCC-Al, FCC-Si, 3C–SiC, and FCC-Al, which indicates that no distinct oxidation occurred in the Al ally matrix during the grinding process even at $v_g = 133.5$ m/s and $v_g = 307.0\,m/s$.

In terms of the source of the O-rich zone, it was not the coolant residue or the debris of the grinding wheel because of the mismatch of the O- and C-elements in their respective distribution maps. As a result, the occurrence of the O-element in the workpiece subsurface was induced by the absorption of the O-element from the environment in the newly-formed cracks and the separated interface between the two components of Al/SiCp MMCs. Therefore, it implies that the O-element distribution map reflected the occurrence of cracks. It can be generally concluded that the workpiece ground at a higher grinding speed was with less damage than at a lower grinding speed according to the reduced O-rich zone in Fig. 7a–c.

### 3.3. Material removal mechanisms of Al alloy matrix and SiC particles

To carry out an in-depth investigation on the features of SSD, bright-field TEM images were mainly employed to investigate the morphology and distribution of dislocations, cracks and other material defects at the subgrain scale. As shown in Fig. 8b–e, the refined Al grains located at different depths from the ground surface in Fig. 8a ($v_g = 30.4$ m/s) were used to investigate the refinement mechanisms. It is evident that the microstructure of the top surface layer as shown in Fig. 8b was

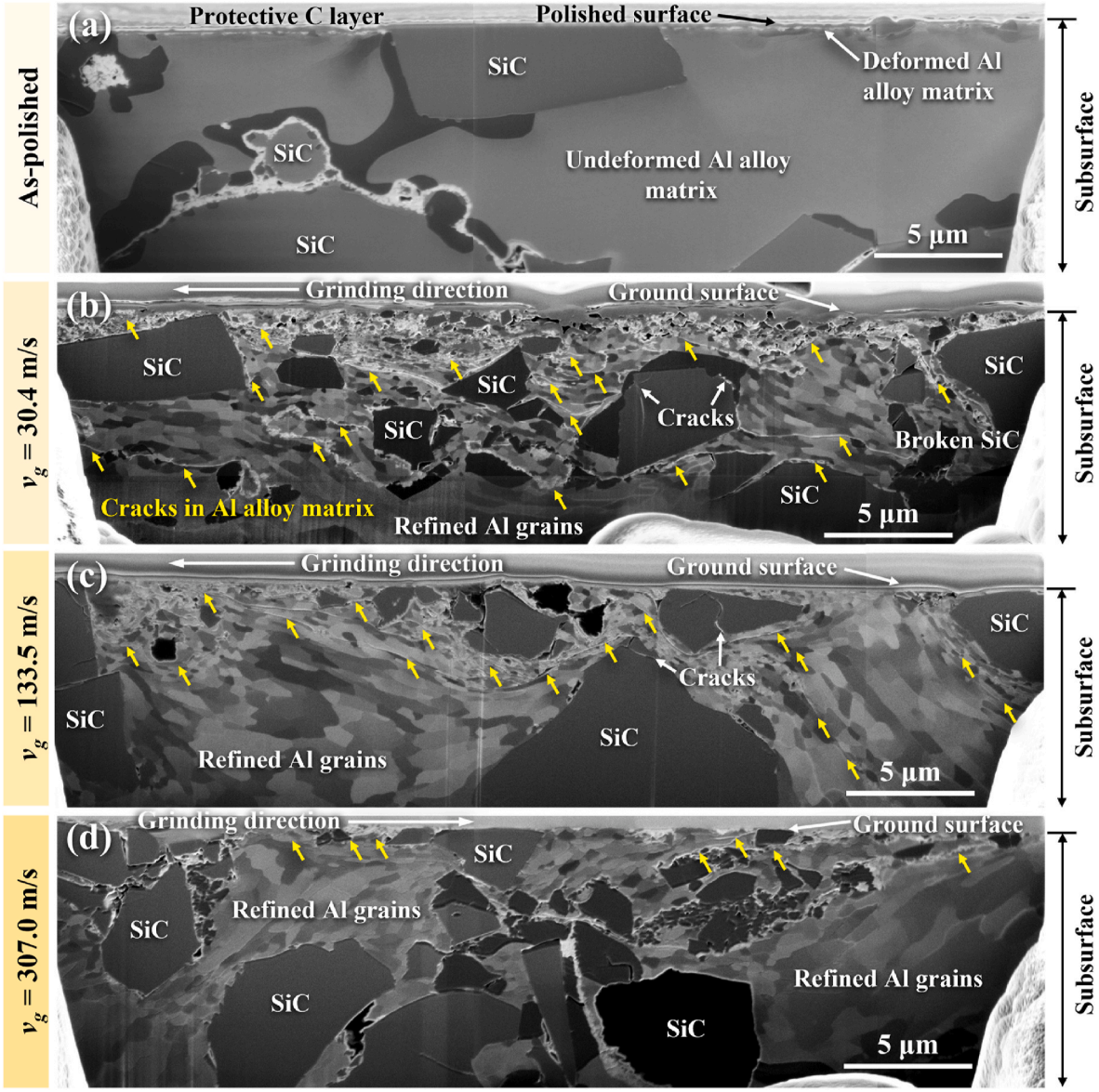


**Fig. 6.** Representative cross-sectional images beneath the workpiece surface after (a) polishing using diamond abrasive papers; (b) grinding at $v_g = 30.4\ m/s$; (c) grinding at $v_g = 133.5\ m/s$, and (d) grinding at $v_g = 307.0\ m/s$. Broken SiC particles surrounded by deformed and refined Al alloy matrix, as well as evident lateral cracks in Al alloy matrix were main features of SSD, which reduced at an increased grinding speed.

characterized by the extremely ultrafine Al grains of ~100 nm in size, in which high-density dislocations were identified near multiple stacking faults. Similarly at a depth of ~1 μm, it shows an Al grain featuring dislocation pile-up near multiple stacking faults in Fig. 8c. Multiple stacking faults impede dislocation climb and cross-slip [29]. It is believed that dislocations pile up at multiple stacking faults, which locally increases the energy so as to drive nucleation of new grains and prevent the existing grains from further growth, following the mechanism of discontinuous dynamic recrystallization (dDRX) [30,31]. Based on the features revealed in Fig. 8b,c, the mechanism of grain refinement can be ascribed to dDRX. At a depth of ~3 μm, two adjacent Al grains with a size of ~300 μm were revealed with distinct dislocation arrays as shown in Fig. 8d, which were typical features of continuous dynamic recrystallization (cDRX). According to the mechanism of cDRX, new grain boundaries formed at dislocation arrays after continuous accumulation of deformation-induced dislocations due to an increase of the sub-boundary misorientation [31]. In Fig. 8e, at a depth of ~5 μm, a grain of ~500 μm in width is identified to possess multiple stacking faults that can store energy for the nucleation and growth of dDRX grains [31]. As a result, both cDRX and dDRX mechanisms took effect in the microstructural evolution of Al grain refinement during grinding at $v_g = 30.4$ m/s, according to the features of the refined Al grains at different depths from the ground surface.

Figs. 9 and 10 revealed SSD of Al grains at different depths in the workpiece ground at $v_g = 133.5$ m/s and $v_g = 307.0$ m/s, respectively. Both the features of cDRX and dDRX mechanisms were identified in the refined Al grains. It is revealed that multiple stacking faults in Figs. 9b,c and 10b were typical features of dDRX whereas the dislocation arrays formed in the interiors and boundaries of the grains in Figs. 9d,e and 10c-e were typical features of cDRX. Although both cDRX and dDRX mechanisms dominated Al refinement for the workpiece ground at different speeds, the occurrence of these two mechanisms were generally associated with the depth from the ground surface. To be specific, dDRX tended to occur in the upper part whereas cDRX tended to dominate the lower part of the ground surface. cDRX is commonly considered as the main mechanism for the grain refinement in Al during plastic deformation [31–33]. Compared with cDRX, dDRX is more difficult to take place in Al because it is hard to achieve sufficiently high

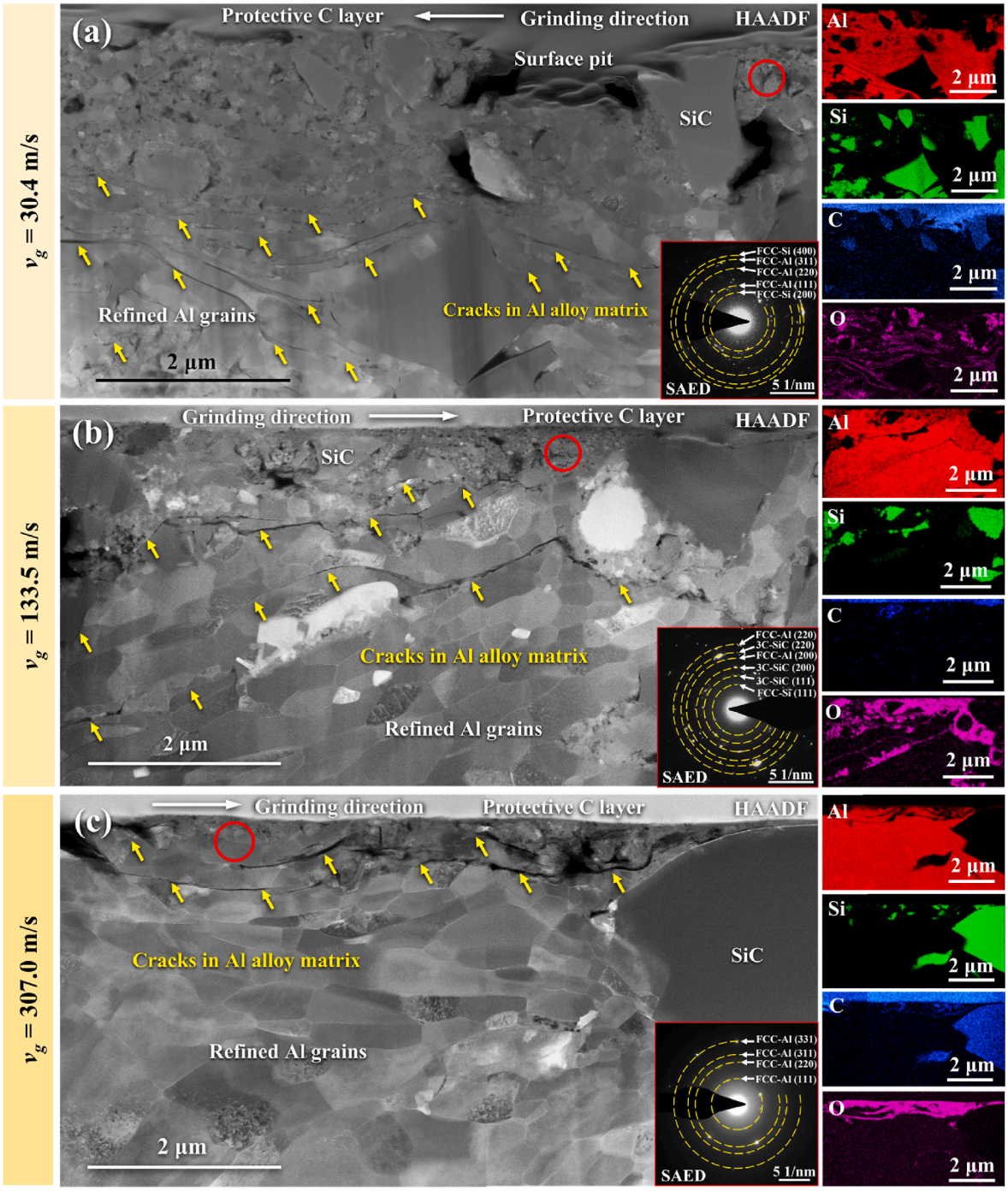


**Fig. 7.** HAADF images, SAED patterns and EDS images of the O-rich zone of the workpiece subsurface after grinding at (a) $v_g = 30.4\ m/s$; (b) $v_g = 133.5\ m/s$, and (c) $v_g = 307.0\ m/s$. The red circles in the O-rich zones indicate the positions for SAED. (For interpretation of the references to colour in this figure legend, the reader is referred to the Web version of this article.)

dislocation densities inside the grains for nucleation [34]. Moreover, a higher temperature of above approximately half the melting point is needed to promote grain refinement during dDRX, while any temperature below the melting point works for cDRX [34]. It indicates that the dDRX in the upper part of the ground surface was likely to result from the high temperature induced by the grinding wheel. However, the depth of the heat-affected zone decreased with increasing the grinding speed according to the reduced depth of the dDRX affected Al grains.

SSD of SiC particles at the superficial layer of ground subsurfaces was investigated using TEM. As shown in Fig. 11a,d,g, the selected regimes ground at the respective speeds featured a string of broken SiC particles located from the ground surface to the workpiece interior, which is considered to be caused by direct knocking of the abrasives during grinding. In this way, all the selected SiC particles were broken during grinding. It is found from the SiC particles in the subsurface ground at $v_g$ = 30.4 m/s that no significant dislocations were identified in the particles apart from some stacking faults in Fig. 11b. For the SiC particle as shown in Fig. 11c, several dislocation kinks formed at the boundary of the SiC particle. In terms of the damage features at $v_g$ = 133.5 m/s, a cluster of dislocations kinked at the boundary of the SiC particle which was likely the location where the SiC particle collision happened, as shown in Fig. 11d–f. When the grinding speed further increased to $v_g$ =

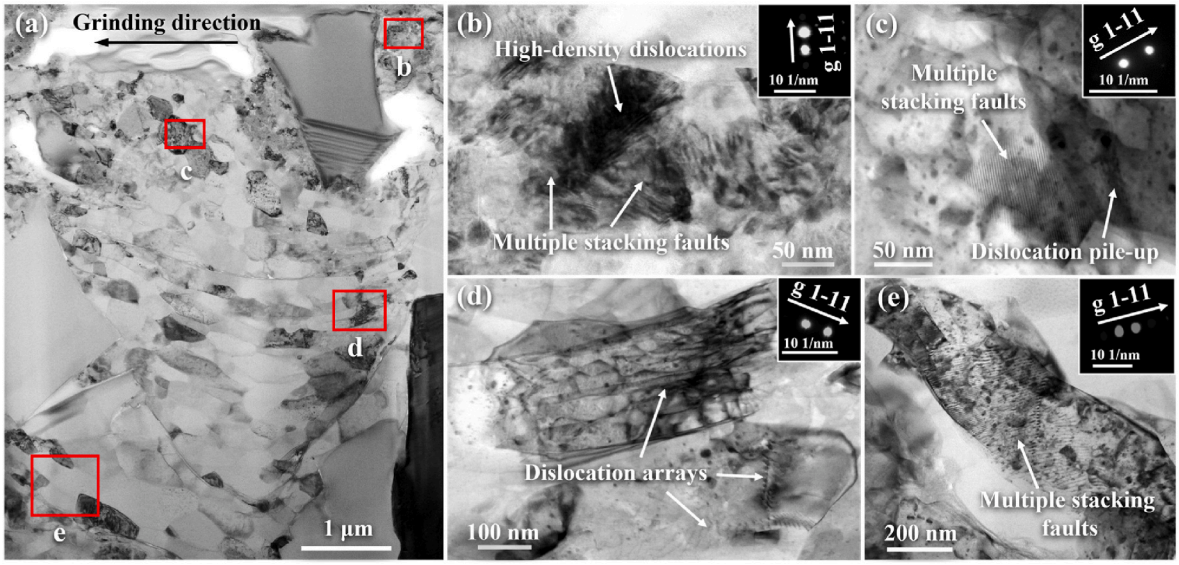


**Fig. 8.** Bright-field TEM images of Al grains in the subsurface of the workpiece ground at $v_g = 30.4$ m/s: (a) subsurface microstructure; (b)–(e) features of dislocations and stacking faults in Al grains along the depth direction from the ground surface. The insets in (b)–(e) display the SAED patterns of the two-beam conditions used for dislocation analysis.

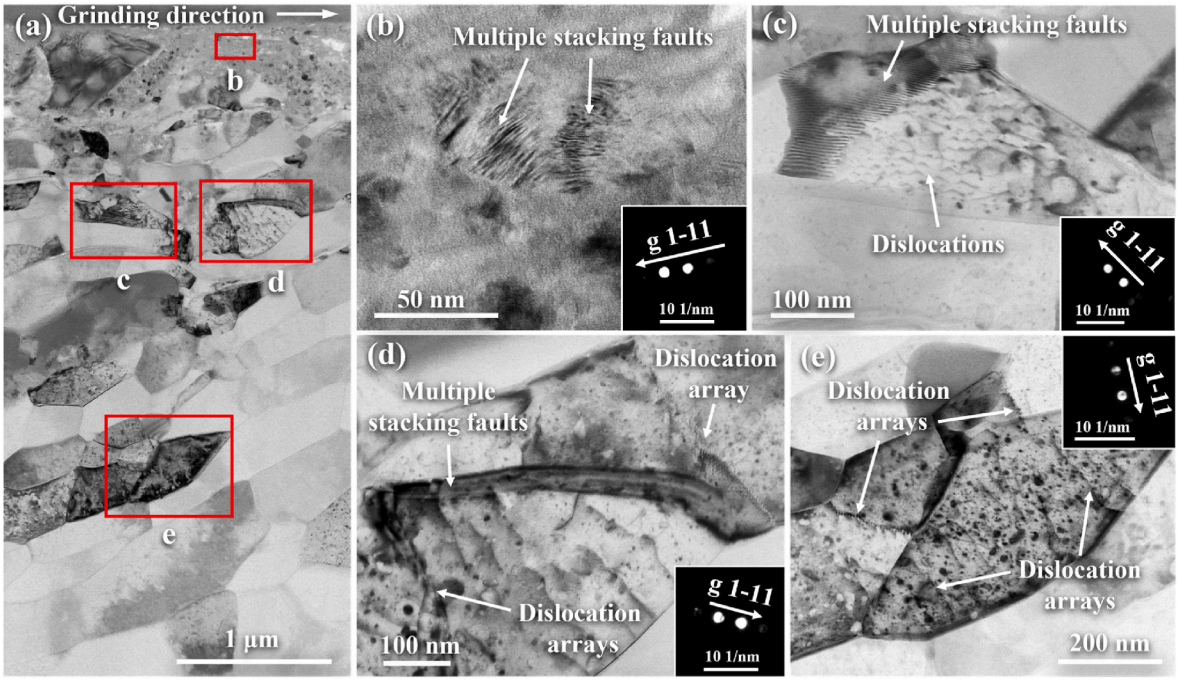


**Fig. 9.** Bright-field TEM images of Al grains in the subsurface of the workpieces ground at $v_g = 133.5$ m/s: (a) subsurface microstructure; (b)–(e) features of dislocations and stacking faults in Al grains along the depth direction from the ground surface. The insets in (b)–(e) display the SAED patterns of the two-beam conditions used for dislocation analysis.

307.0 m/s, the phenomena similar to those recorded in Fig. 11d–f were revealed, i.e., distinct dislocations tangles appeared at the boundary of the SiC particle in Fig. 11g–i. In comparison with the SSD features revealed in the workpiece subsurface ground at $v_g = 30.4$ m/s, the distinctly denser dislocation kinks formed at the boundary of the SiC particle in those ground at $v_g = 133.5$ m/s and $v_g = 307.0\ m/s$ at the same depth from the ground surface, indicating an increased ductility of SiC particles.

## 4. Discussion

Comparing with the conventional machining methods, HSG is a more complicated process which is mainly governed by thermal effect, size effect, and strain-rate effect. These effects always interplay and hard to be accurately measured in a practical HSG process. Therefore, it is difficult to decouple them and separately analyze the individual effects. Moreover, the property discrepancies between the two components of Al/SiCp MMCs further increases uncertainty of an HSG process and difficulty in analyzing the material removal mechanisms. This study generally retains the original SSD induced in a grinding process by

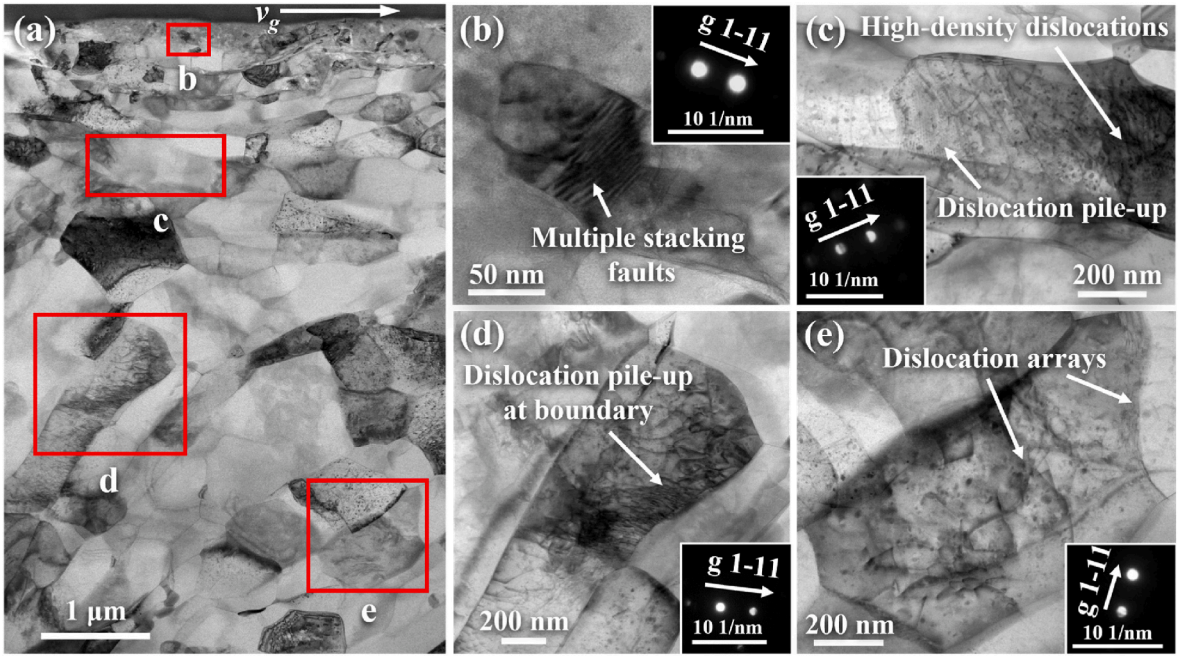


**Fig. 10.** Bright-field TEM images of Al grains in the subsurface of the workpieces ground at $v_g$ = 307.0 m/s: (a) subsurface microstructure; (b)–(e) features of dislocations and stacking faults in Al grains along the depth direction from the ground surface. The insets in (b)–(e) display the SAED patterns of the two-beam conditions used for dislocation analysis.

exploiting the merits of FIB and TEM. Based on the comprehensive SSD features revealed at different grinding speeds, this study attempts to analyze the thermal effect, size effect, and strain-rate effect on surface integrity and material removal mechanisms of Al/SiCp MMCs in HSG.

As for the thermal effect, it is difficult to analyze its influence on grinding of Al/SiCp MMCs because the transient temperature in the grinding zone is difficult to directly measure and the heat conduction in Al/SiCp MMCs is extensively affected by SiC particles distribution. Since any change in workpiece subsurface microstructure is a combined result of surface transient high temperature and heat conduction, the microstructural changes can be employed to indirectly reflect the influence of thermal effect. It is recognized that a higher temperature is beneficial to promoting O-element diffusion into the workpiece subsurface [35]. However, if the distribution of the O-rich zone in the workpiece subsurface is governed by grinding-induced surface temperature, the content of the O-element should gradually reduce from the ground workpiece surface rather than changes abruptly to form a clear demarcation line as shown in Fig. 7a–c. It indicates that grinding-induced surface temperature is not pronounced enough to dominate the distribution of the O-rich zone. The distribution of the O-rich zone is closely associated with subsurface cracks due to the absorption of the O-element from the environment.

Moreover, the depth of a heat-affected zone is generally decreased with increasing the grinding speed according to the reduced depth of the dDRX affected Al grains. In addition, other research concerning thermal effect in HSG can be a useful reference. In order to clarify the influence of thermal effect under the ground surface, Guo et al. [24] established a finite element model based on the Johnson-Cook model for HSG of Al6061T6 alloy. They found that although both the surface temperature and temperature gradient increased with increasing the grinding speed, the high temperature gradient was confined in the superficial surface layer, reflecting a reduced depth of heat-effected zone at an increased grinding speed. This result can also be adopted to explain the mitigated thermal effect in the workpiece subsurface of Al/SiCp MMCs in this study.

The size effect in grinding often refers to the phenomenon that deformation behaviors of a workpiece material change with reducing the thickness of maximum undeformed chip at an increase grinding speed. The strain-rate effect in grinding indicates that at a given depth of grinding, responses of a workpiece material to grinding vary with strain-rate as grinding speed increases. In this study, the influence of these two effects is separately discussed for grinding of ductile Al alloy matrix and brittle SiC particles. For grinding of the ductile Al alloy matrix, an increased grinding speed always causes two different results. On one hand, the reduced maximum undeformed chip thickness at an increased grinding speed favors dislocation movement and further deformation as a result of reduced flow stress [36]. On the other hand, a higher grinding speed increases the yield strength of Al alloy matrix in the grinding zone, resulting in strain-rate hardening [37–39]. For grinding of brittle SiC particles, an increased grinding speed also causes two different results. On one hand, the size effect facilitates brittle-to-ductile transition of SiC [40], which implies that SiC becomes more ductile when it is machined at a significantly reduced depth of cut. On the other hand, a higher strain-rate enhances the brittleness of SiC particles [41,42]. As a result, an increased grinding speed induced different influences on the Al alloy matrix and SiC particles from two different perspectives, i.e., the size effect is to improve the ductility of Al alloy matrix and SiC particles, whereas the strain-rate effect tends to improve brittleness of these two components. A paradox is thus formed, i.e., the size effect and the strain-rate effect are the two competing factors that dominate material responses to grinding. Therefore, it is feasible to determine the specific influences of the size effect and the strain-rate effect according to the practical material responses on ductility or brittleness for these two components of Al/SiCp MMCs in HSG.

At a higher grinding speed, plastic deformation of the Al alloy matrix in the workpiece subsurface is distinctly mitigated, as indicated by larger Al grains and shallower lateral cracks in the Al alloy matrix shown in Fig. 7a–c, which indicates that the strain-rate effect prevails for the Al alloy matrix in HSG of Al/SiCp MMCs as a result of reduced ductility. On the other hand, much denser dislocation kinks formed at the boundary of the SiC particle implies the increased ductility at an increased grinding speed, as shown in Fig. 11. It indicates that size effect plays the dominant role for SiC particles in HSG of Al/SiCp MMCs. Since ductility of the Al alloy matrix is weakened in HSG, the movement of the SiC particles is

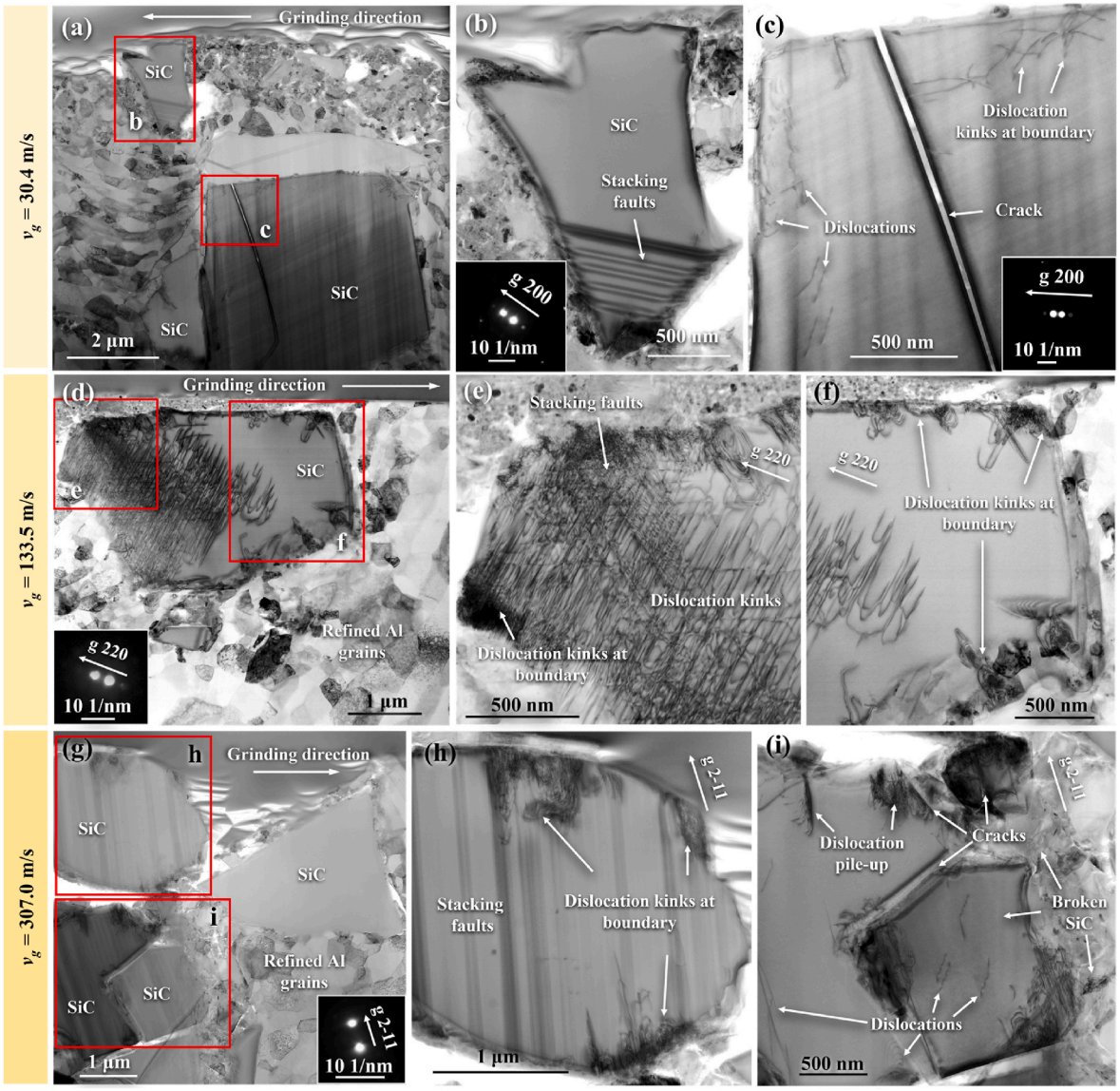


**Fig. 11.** Bright-field TEM images of SiC particles in the subsurface of the workpieces ground at (a)–(c) $v_g = 30.4\,m/s$; (d)–(f) $v_g = 133.5\,m/s$; (g)–(i) $v_g = 307.0\,m/s$. The insets in (b)–(d), and (g) display the SAED patterns of the two-beam conditions used for dislocation analysis.

hence hindered by the hardened Al alloy matrix. As a result, dislocations kink at SiC particle boundary as a result of stress self-accommodation when the SiC particles are impacted by abrasives in HSG. In general, HSG enhances hardness of the ductile Al alloy matrix and reduces the brittleness of the hard SiC particles, which facilitates reducing the property differences between these two components. Therefore, an improved surface integrity of Al/SiCp MMCs is realized by reducing the property discrepancies of the two components through HSG.

Based on the variations of the surface defects and SSD features with respect to different grinding speeds, a schematic diagram reflecting the overall surface integrity of the ground Al/SiCp MMCs is presented in Fig. 12. When Al/SiCp MMCs are ground at a low speed, the two components show different responses because of the great property discrepancies. The SiC particles tend to be pulled out or pushed away to generate surface pits; surface smearing of the Al alloy matrix occurs due to severe plastic deformation. These two responses collectively lead to poor surface quality.

As for the formation of SSD, SiC particles are inclined to be broken into small pieces when contacting the wheel abrasives, thus generating cracks and stacking faults within the particles in terms of energy dissipation. For the Al alloy matrix, some new grains form due to an increased sub-boundary misorientation brought by a continuous accumulation of the deformation-induced dislocations following the mechanism of cDRX. On the other hand, abundant dislocations are initiated and accumulated in some Al grains in the superficial layer of the ground subsurface due to an intense plastic deformation and higher temperature. These dislocations evolve as new crystal nuclei and gradually grow into multiple grains, thus leading to Al grain refinement following the mechanism of dDRX. Moreover, the fractured SiC particles hinder the growth of the Al grains and also promote grain refinement [1]. Since the topmost layer of the ground surface is subjected to the highest strain and temperature, Al grain refinement and SiC particle fragmentation are more likely to occur in this layer. With increasing the depth from the ground surface, these two responses are gradually weakened until reaching the bulk material.

As a result, three different layers in the subsurface of the ground workpiece can be identified, as shown in Fig. 12. The topmost is a hybrid layer which is featured with the refined Al grains and the fragmentary SiC particles at a scale of nanometers. The refined Al grains are mostly induced by the mechanism of dDRX due to the highest strain and temperature. Below the hybrid layer, fewer refined Al grains and larger broken SiC particles emerge in the plastic flow layer because of the

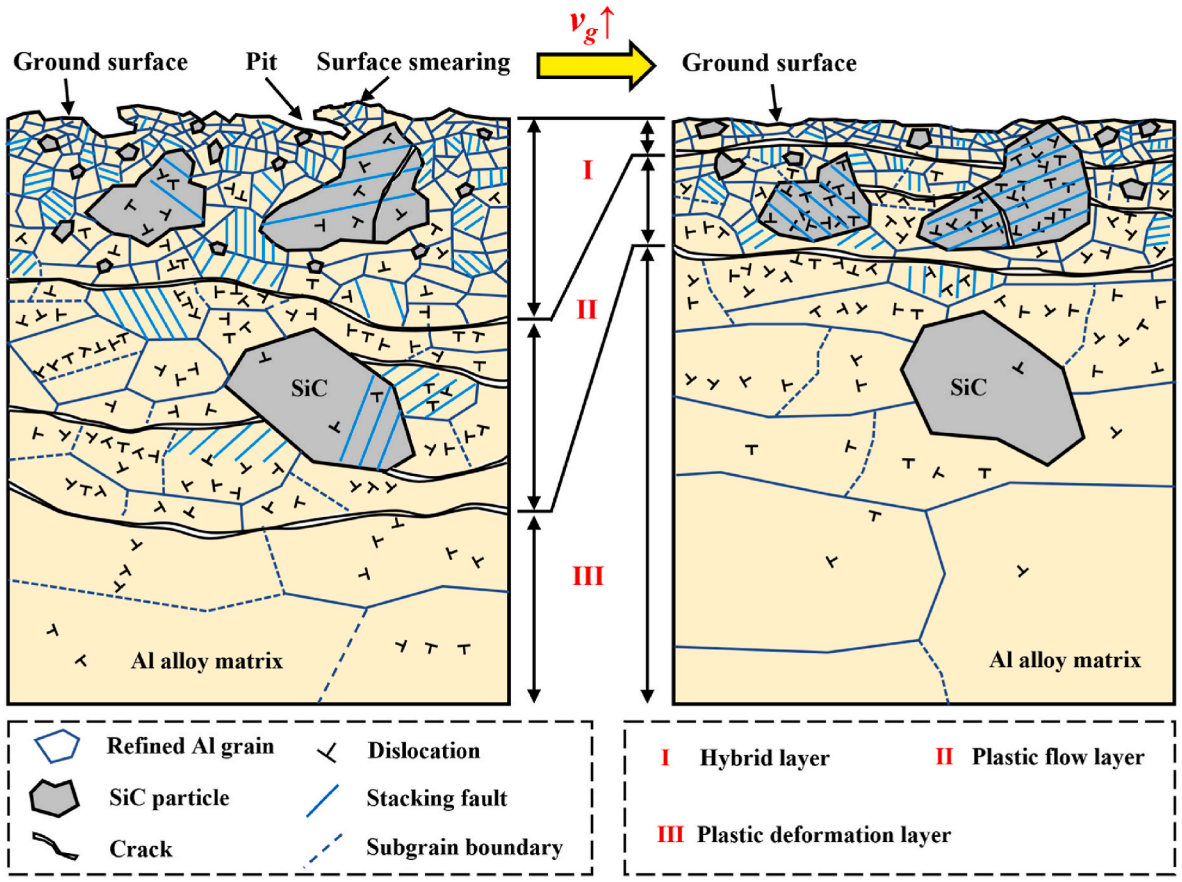


**Fig. 12.** Schematic of subsurface microstructural variation with grinding speed.

relatively less disturbance from the grinding wheel, in which the distinct lateral cracks are the typical features in the Al alloy matrix. These cracks in the Al alloy matrix are resulted from the shearing of the migrated SiC particles. Along the depth direction from the ground surface, Al grain refinement and SiC particle fragmentation are further weakened in the plastic deformation layer, in which the elongated Al grains around the migrated SiC particles are the major features and no evident broken SiC particles are found in this layer. cDRX prevails in the plastic flow layer and plastic deformation layer due to less heat conducted from the ground surface.

At an increased grinding speed, the alteration of the corresponding surface defects and SSD features are subjected to the synergetic influences of thermal effect, size effect, and strain-rate effect. With increasing the grinding speed, surface quality is improved due to smaller surface pits and reduced grinding scratches. The subsurface microstructure can be divided into three layers, but the corresponding depths of hybrid layer and plastic deformation layer are relatively shallower as a result of reduced influence of heat and strain in HSG compared with that in low-speed grinding. An improved surface integrity of Al/SiCp MMCs is thus realized in HSG. The plastic deformation of the Al alloy matrix is dominated by the strain-rate effect, which is evidenced by the larger Al grains and shallower lateral cracks in the Al alloy matrix in HSG. However, the size effect plays the dominant role for SiC particles due to the increased ductility since much denser dislocation kinks formed at the boundaries of the SiC particles in HSG.

Finally, more work is necessary to reveal a larger cross-sectional area of a ground workpiece for classifying the types of SSD and determining the boundary of different types of SSD. In addition, more efforts are also needed to assess the effects of size, shape, distribution, and percentage of the reinforced SiC particles on surface integrity and material removal mechanisms in HSG of Al/SiCp MMCs.

## 5. Conclusions

To achieve high-efficiency, high-accuracy, and low-damage machining of Al/SiCp MMCs, HSG is performed at a speed up to 307.0 m/s, and the corresponding surface integrity and material removal mechanisms are investigated considering surface morphology, surface roughness, and SSD at different scales. The alteration of surface defects and SSD with increasing the grinding speed is clarified. For the first time, the material removal mechanisms of Al/SiCp MMCs are uncovered and clarified considering thermal effect, size effect, and strain-rate effect based on comprehensive and multiscale surface defects and SSD characterization methods. Major conclusions are summarized as follows:

(1) A higher grinding speed improves surface quality, which is evidenced by the reduced grinding scratches, surface pits, and surface roughness.
(2) Both cDRX and dDRX mechanisms govern Al grain refinement in grinding of Al/SiCp MMCs. dDRX is inclined to occur in the upper part of a ground surface due to more plastic deformation and higher temperature.
(3) The distribution of the O-rich zone is closely associated with subsurface cracks. The workpiece ground at a higher grinding speed is with less damage than at a lower grinding speed due to the reduced O-rich zone.
(4) Three different layers in the subsurface below ground workpiece are identified based on various features. The topmost hybrid layer features the refined Al grains and fragmentary SiC particles at a scale of nanometers. Below the hybrid layer, lateral cracks are found in the Al alloy matrix, forming a crack layer. Underneath the crack layer is the plastic deformation layer, refined and

elongated Al grains are observed around the migrated SiC particles. The depths of hybrid layer and plastic deformation layer in HSG are relatively narrower compared to that in low-speed grinding.

(5) The range of plastic deformation of the Al alloy matrix is suppressed in HSG. Distinctly denser dislocation kinks formed at the boundary of SiC particles in HSG indicate the increased ductility of SiC particles. The responses of these two components in HSG facilitate reducing the property discrepancies between these two components. Therefore, improved surface integrity of Al/SiCp MMCs is realized through HSG.

## Credit author statement

**Sai Guo**: Conceptualization, Methodology, Characterization, Data analysis, Writing-Original Draft. **Shouxiang Lu**: Data analysis, Review & Editing; **Bi Zhang**: Conceptualization, Resources, Review & Editing, Supervision. **Chi Fai Cheung**: Resources, Review & Editing, Supervision.

## Declaration of competing interest

The authors declare that they have no known competing financial interests or personal relationships that could have appeared to influence the work reported in this paper.

## Data availability

The authors do not have permission to share data.

## Acknowledgements

This work is supported by Shenzhen Science and Technology Innovation Commission for the project numbered KQTD20190929172505711, JSGG20210420091802007, and by Shenzhen Key Laboratory of Cross-Scale Manufacturing Mechanics of Southern University of Science and Technology under ZDSYS20200810171201007. The authors also wish to acknowledge the assistance from SUSTech Core Research Facilities. Sai Guo would like to extend his sincere thanks to Miss Jiasi Luo for her assistance in TEM operation and dislocation analysis.

## References

[1] X. Han, D. Xu, D. Axinte, Z. Liao, H.N. Li, On understanding the specific cutting mechanisms governing the workpiece surface integrity in metal matrix composites machining, J. Mater. Process. Technol. 288 (2021), 116875.
[2] Z. Liao, A. Abdelhafeez, H. Li, Y. Yang, O.G. Diaz, D. Axinte, State-of-the-art of surface integrity in machining of metal matrix composites, Int. J. Mach. Tool Manufact. 143 (2019) 63–91.
[3] Y. Fan, Y. Xu, Z. Hao, J. Lin, Cutting deformation mechanism of SiCp/Al composites based on strain gradient theory, J. Mater. Process. Technol. 299 (2022), 117345.
[4] N. Suresh Kumar Reddy, S. Kwang-Sup, M. Yang, Experimental study of surface integrity during end milling of Al/SiC particulate metal–matrix composites, J. Mater. Process. Technol. 201 (1) (2008) 574–579.
[5] F. Klocke, S.L. Soo, B. Karpuschewski, J.A. Webster, D. Novovic, A. Elfizy, D. A. Axinte, S. Tönissen, Abrasive machining of advanced aerospace alloys and composites, CIRP Annals 64 (2) (2015) 581–604.
[6] C. Zhu, P. Gu, Y. Wu, D. Liu, X. Wang, Surface roughness prediction model of SiCp/Al composite in grinding, Int. J. Mech. Sci. 155 (2019) 98–109.
[7] M. El-Gallab, M. Sklad, Machining of Al/SiC particulate metal-matrix composites: Part I: tool performance, J. Mater. Process. Technol. 83 (1) (1998) 151–158.
[8] A. Di Ilio, A. Paoletti, A comparison between conventional abrasives and superabrasives in grinding of SiC-aluminium composites, Int. J. Mach. Tool Manufact. 40 (2) (2000) 173–184.
[9] Z. Yang, L. Zhu, G. Zhang, C. Ni, B. Lin, Review of ultrasonic vibration-assisted machining in advanced materials, Int. J. Mach. Tool Manufact. 156 (2020), 103594.
[10] A. Manna, B. Bhattacharayya, A study on machinability of Al/SiC-MMC, J. Mater. Process. Technol. 140 (1) (2003) 711–716.
[11] C. Liu, W. Ding, T. Yu, C. Yang, Materials removal mechanism in high-speed grinding of particulate reinforced titanium matrix composites, Precis. Eng. 51 (2018) 68–77.
[12] L. Ceschini, G. Minak, A. Morri, Tensile and fatigue properties of the AA6061/20vol% Al2O3p and AA7005/10vol% Al2O3p composites, Compos. Sci. Technol. 66 (2) (2006) 333–342.
[13] S. Kannan, H.A. Kishawy, Surface characteristics of machined aluminium metal matrix composites, Int. J. Mach. Tool Manufact. 46 (15) (2006) 2017–2025.
[14] L. Gu, M. Wang, C. Duan, On adiabatic shear localized fracture during serrated chip evolution in high speed machining of hardened AISI 1045 steel, Int. J. Mech. Sci. 75 (2013) 288–298.
[15] A. Pramanik, L.C. Zhang, J.A. Arsecularatne, An FEM investigation into the behavior of metal matrix composites: tool–particle interaction during orthogonal cutting, Int. J. Mach. Tool Manufact. 47 (10) (2007) 1497–1506.
[16] X. Teng, W. Chen, D. Huo, I. Shyha, C. Lin, Comparison of cutting mechanism when machining micro and nano-particles reinforced SiC/Al metal matrix composites, Compos. Struct. 203 (2018) 636–647.
[17] A. Pramanik, L.C. Zhang, J.A. Arsecularatne, Machining of metal matrix composites: effect of ceramic particles on residual stress, surface roughness and chip formation, Int. J. Mach. Tool Manufact. 48 (15) (2008) 1613–1625.
[18] J.P. Davim, Design of optimisation of cutting parameters for turning metal matrix composites based on the orthogonal arrays, J. Mater. Process. Technol. 132 (1) (2003) 340–344.
[19] J. Xiang, S. Pang, L. Xie, X. Hu, S. Peng, T. Wang, Investigation of cutting forces, surface integrity, and tool wear when high-speed milling of high-volume fraction SiCp/Al6063 composites in PCD tooling, Int. J. Adv. Manuf. Technol. 98 (5) (2018) 1237–1251.
[20] O. Gavalda Diaz, G. Garcia Luna, Z. Liao, D. Axinte, The new challenges of machining Ceramic Matrix Composites (CMCs): Review of surface integrity, Int. J. Mach. Tool Manufact. 139 (2019) 24–36.
[21] B. Zhang, J. Yin, The 'skin effect' of subsurface damage distribution in materials subjected to high-speed machining, Int. J. Extreme Manufact. 1 (1) (2019), 012007.
[22] X. Yang, B. Zhang, Material embrittlement in high strain-rate loadings, Int. J. Extreme Manufact. 1 (2) (2019), 022003.
[23] J. Shimizu, L.B. Zhou, H. Eda, Simulation and experimental analysis of super high-speed grinding of ductile material, J. Mater. Process. Technol. 129 (1) (2002) 19–24.
[24] S. Guo, J. Zhang, Q. Jiang, B. Zhang, Surface integrity in high-speed grinding of Al6061T6 alloy, CIRP Annals (2022). In press.
[25] A. Choudhary, S. Paul, Surface generation in high-speed grinding of brittle and tough ceramics, Ceram. Int. 47 (21) (2021) 30546–30562.
[26] J. Chen, J. Shen, H. Huang, X. Xu, Grinding characteristics in high speed grinding of engineering ceramics with brazed diamond wheels, J. Mater. Process. Technol. 210 (6) (2010) 899–906.
[27] Q. Wu, W. Xu, L. Zhang, Machining of particulate-reinforced metal matrix composites: an investigation into the chip formation and subsurface damage, J. Mater. Process. Technol. 274 (2019), 116315.
[28] X. Rao, F. Zhang, Y. Lu, X. Luo, F. Chen, Surface and subsurface damage of reaction-bonded silicon carbide induced by electrical discharge diamond grinding, Int. J. Mach. Tool Manufact. 154 (2020), 103564.
[29] W.W. Jian, G.M. Cheng, W.Z. Xu, H. Yuan, M.H. Tsai, Q.D. Wang, C.C. Koch, Y. T. Zhu, S.N. Mathaudhu, Ultrastrong Mg alloy via nano-spaced stacking faults, Mater. Res. Lett. 1 (2) (2013) 61–66.
[30] W. Zhang, Q. Wei, W.T. Huo, J.W. Lu, J.J. Hu, Y.S. Zhang, Dynamic recrystallization in nanocrystalline AZ31 Mg-alloy, Vacuum 143 (2017) 236–240.
[31] S. Wei, H. Zhang, C. Tangpatjaroen, J. Tarnsangpradit, A.D. Usta, M. Eriten, J. H. Perepezko, I. Szlufarska, Wear-induced microstructural evolution of ultra-fine grained (UFGs) aluminum, Acta Mater. 209 (2021), 116787.
[32] H. Hallberg, M. Wallin, M. Ristinmaa, Modeling of continuous dynamic recrystallization in commercial-purity aluminum, Mater. Sci. Eng. A 527 (4) (2010) 1126–1134.
[33] Y.J. Chen, H.J. Roven, S.S. Gireesh, P.C. Skaret, J. Hjelen, Quantitative study of grain refinement in Al–Mg alloy processed by equal channel angular pressing at cryogenic temperature, Mater. Lett. 65 (23) (2011) 3472–3475.
[34] T. Sakai, A. Belyakov, R. Kaibyshev, H. Miura, J.J. Jonas, Dynamic and post-dynamic recrystallization under hot, cold and severe plastic deformation conditions, Prog. Mater. Sci. 60 (2014) 130–207.
[35] C.-h. Yin, Y.-l. Liang, Y. Liang, W. Li, M. Yang, Formation of a self-lubricating layer by oxidation and solid-state amorphization of nano-lamellar microstructures during dry sliding wear tests, Acta Mater. 166 (2019) 208–220.
[36] M.W. Fu, J.L. Wang, Size effects in multi-scale materials processing and manufacturing, Int. J. Mach. Tool Manufact. 167 (2021), 103755.
[37] C.Y. Chiem, J. Duffy, Strain rate history effects and observations of dislocation substructure in aluminum single crystals following dynamic deformation, Mater. Sci. Eng. 57 (2) (1983) 233–247.
[38] F. Barlat, M.V. Glazov, J.C. Brem, D.J. Lege, A simple model for dislocation behavior, strain and strain rate hardening evolution in deforming aluminum alloys, Int. J. Plast. 18 (7) (2002) 919–939.
[39] M. Scapin, A. Manes, Behaviour of Al6061-T6 alloy at different temperatures and strain-rates: experimental characterization and material modelling, Mater. Sci. Eng. A 734 (2018) 318–328.

[40] J. Cao, Y. Wu, D. Lu, M. Fujimoto, M. Nomura, Material removal behavior in ultrasonic-assisted scratching of SiC ceramics with a single diamond tool, Int. J. Mach. Tool Manufact. 79 (2014) 49–61.
[41] D.E. Grady, M.E. Kipp, Mechanisms of dynamic fragmentation: factors governing fragment size, Mech. Mater. 4 (3) (1985) 311–320.
[42] S.M. Zakir, W. Zhen, S. Tao, L. Yulong, Z. Fenghua, A. Sohail, U.A. Dar, High rate response and dynamic failure of aluminosilicate glass under compression loading, Procedia Struct. Integr. 13 (2018) 1244–1249.